AB INITIO BASED MONTE CARLO MODEL OF PHASE TRANSFORMATIONS IN FERROMAGNETIC SHAPE MEMORY ALLOYS

BY

BRIAN BLANKENAU

THESIS

Submitted in partial fulfillment of the requirements
for the degree of Master of Science in Mechanical Science and Engineering
in the Graduate College of the
University of Illinois at Urbana-Champaign, 2018

Urbana, Illinois

Adviser:

Professor Elif Ertekin

ABSTRACT

We present a computational framework for describing and predicting the phase transformation behavior of ferromagnetic shape memory alloys (FSMAs). This framework is intended to aid in the discovery of new FSMAs and optimize desired properties of existing FSMAs for engineering applications such as solid state refrigeration. Predicting the phase transformation behavior in theses alloys is necessary to determine the degree to which they will exhibit the magnetocaloric effect (MCE), which is a promising alternative to conventional refrigeration mechanisms. Our framework consists of a combination of *ab-initio* simulations and Monte Carlo models which allow an alloy to be examined across its phase space without the need for any empirical parameters. In this document, we focus on the Heusler alloy $Ni_{50}Mn_{50-x}In_x$ as it has already been the subject of substantial experimental and computational work. This material serve as a benchmark for the development of our method. In the remainder of this document we will discuss the framework and how the *ab-initio* and Monte Carlo methods are integrated.

To my parents, for their love and support.

ACKNOWLEDGMENTS

I would like to thank my advisor, Dr. Elif Ertekinn, for her patience, mentorship, and support, without which this work would not be possible. I would also like to acknowledge the support of the National Science Foundation and the resources provided by the the University of Illinois Campus Computing Cluster.

TABLE OF CONTENTS

LIST OF FIGURES

CHAPTER 1

INTRODUCTION

Refrigeration and air conditioning are significant consumers of the world's energy supply. As countries around the world continue to develop, the demand for these technologies will only increase and further strain our already fragile energy supply and infrastructure. Additionally, many common refrigeration mechanisms require refrigerants that are harmful to the environment. This highlights the fact that more energy efficient refrigeration technologies could have a serious positive impact on a large portion of society and serve to help mediate the emissions of greenhouse gases. Magnetocaloric materials such as ferromagnetic shape memory alloys (FSMA) are promising alternatives to conventional refrigeration methods [5, 6, 7].

The Magnetocaloric effect, or MCE, is associated with a decrease in a material's temperature when it is subjected to a changing magnetic field [8]. FSMAs can, in certain insistences, exhibit an extremely large MCE because of a coupling between a changing internal magnetic order and a change in the crystallographic phase of the alloy. Currently, the limit to developing MCE refrigeration lies with the performance of the the MCE materials themselves [5]. The degree to which FSMAs exhibit the MCE is highly dependent on the alloy composition. Small changes in atomic percent of various elements can cause large changes in the temperature difference (ΔT) associated with a changing magnetic field [2]. This makes the search for new and improved FSMAs for MCE applications rather cumbersome from an experimental standpoint.

In an effort to speed up the materials discovery process, we introduce a computational framework for predicting the phase change behavior and temperature change associated with a change in magnetic field. Eventually, we hope to be able to extend this framework to a high throughput tool for discovering new FSMAs and optimizing their compositions to maximize MCE performance.

This framework is divided into three main tasks: Generating raw data through *ab-initio* simulations, using the data to parametrize a spin lattice model, and running the model in a Monte Carlo simulation to observe its behavior as a function of temperature (T) and applied magnetic field (B). From the data produced in the final step we can use the Clausius-Clapeyron relation to determine the temperature change associated with a sudden change in an applied magnetic field. This thesis will discuss each of these steps, with the majority of the focus on step one.

CHAPTER 2

OVERVIEW OF KEY CONCEPTS

In order to ensure that the main contributions and conclusions of this thesis are easily understood, it is necessary to present a brief overview of several key concepts relating to the nomenclature, mathematics, and physics used.

2.1 Martensitic Phase Transformations

The driver behind all FSMA properties of interest is the martensitic phase transformation. This phase transformation is most commonly associated with steel, specifically with quenching. However, it is often used to describe any phase transformation that takes place in a diffusionless and coordinated manner. In most of these cases, the high temperature parent phase is a cubic $L2_1$ structure referred to as "austenite." The term "martensite" is used to describe the product of the transformation. As a diffusionless transformation, no atom moves by more than a single inter-atomic spacing during the transformation. Consequently, there is no local or global change in composition associated with a martensitic transformation, only a change in crystal structure. The relative coordination of every atom is preserved during the transformation; therefore there is typically a strain associated with the change in crystal structure. The propagation of this strain from a nucleation point is usually what spreads the transformation though the system.

For the engineering applications of FSMAs, martensitic phase transformation cycles are of primary importance. When a FSMA sample is transformed back and forth between austenite and martensite, hysteresis effects are observed. This is not unusual for systems having a complex phase space profile with multiple, competitive local minima, such as FSMAs [9]. This hysteresis is illustrated in Figure 2.1 for the case of a percent martensite vs. temperature measurement.

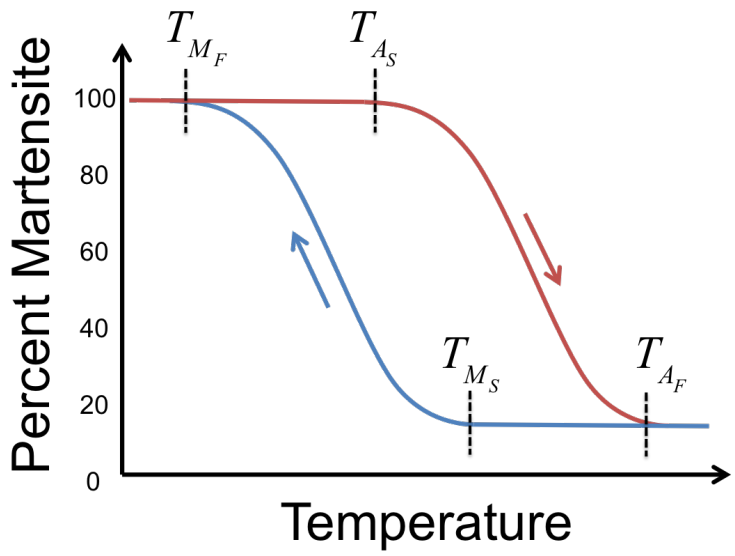

Figure 2.1: Hysteresis loop for a martensitic phase transformation. The path in red indicates the sample is being heated while the path in blue indicates the sample is being cooled.

Starting from the low temperature martensite phase, the sample is heated until the phase transformation begins. This is referred to as the austenite starting temperature or T_{A_S}. The transformation may begin at different points in the sample and begin to nucleate. The temperature at which the transformation is complete is known as the austenite finishing temperature or T_{A_F}.

If the sample is cooled starting from an austenite phase, it will not begin transforming back into martensite at T_{A_F}. Instead it will remain in the metastable austenite state until it is cooled below a critical temperature known as the martensite starting temperature, T_{M_S}, and continue to transform until it has been cooled to the point where it has fully transformed, the martensite finishing temperature T_{M_F}.

For the case of a polycrystalline sample, the transformation will nucleate from separate grains until the entire sample has transformed to austenite. For monocrystalline systems the transformation is much more abrupt than the polycrystalline case, with starting and finishing temperatures closer together. In this case the difference is disregarded entirely and the critical temperatures are simply referred to as austenite and martensite transition temperatures T_A and T_M.

The area enclosed by the heating and cooling cycles is directly proportional to the energy dissipated in the phase transformation [9]. The dependence of the phase transformation behavior on the directionality of the transformation is not limited to strain vs. temperature, but also can be seen in all the phase transformation behaviors of FSMAs. This hysteresis is important for determining the FSMAs performance for the shape memory and pseudoelastic effects [5, 6, 7, 9, 10].

2.2 Shape Memory Alloys

Shape memory alloys or SMAs refer to any of a number of alloys that can exhibit the shape memory effect. This is a phase change phenomenon that allows a deformed alloy sample to return to its undeformed shape upon the application of heat. Due to their unique properties, SMAs can seem like something out of science fiction. Indeed, a metal that can remember its shape brings to mind images a of certain killer robot. However the real world applications of this particular material are much less sinister, ranging from aviation to actuators and medical devices [11].

2.2.1 Discovery

Like many of the most interesting discoveries in science and engineering, shape memory alloys were discovered somewhat by accident. In the early 1960's, Buehler and colleagues at the US Naval Ordnance Laboratory were searching for appropriate alloys to be used in reentry vehicles [12]. Among the potential candidates was NiTi. Buehler became interested in NiTi in particular after it appeared to have unusual acoustic damping properties associated with temperature change [12]. A sample of NiTi was brought to a meeting where the the status of the NiTi project was to be discussed. During the meeting, Buehler's colleague, Wiley, began bending the sample and heating it with his lighter. To his surprise, the heated sample reverted to its pre-deformed shape. Further research later confirmed that the mechanism for this behavior was a martensitic phase transformation. Over the decades, this mechanism has been shown to give rise to many other intriguing properties of SMAs. They include the two-way shape memory effect, pseudoelastic

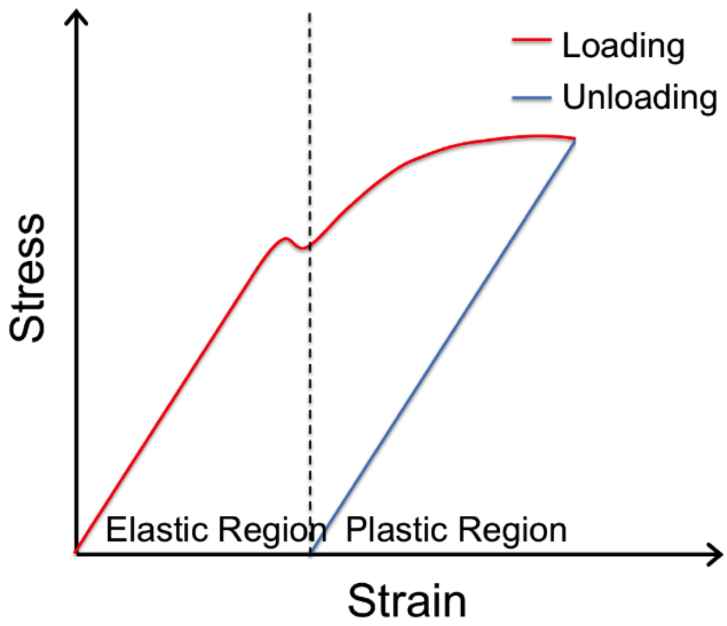

Figure 2.2: A Stress vs. Strain plot for a typical sample undergoing plastic deformation in a loading (red) and unloading (blue) cycle.

effect, and both the elastocaloric and magnetocaloric effects.

2.2.2 Psudoelastic Effect

The easiest way to understand how the martensitic phase transformation gives rise to some of the SMAs unusual properties is by starting with the pseudoelastic effect. When bending a sample of NiTi wire it feels more like a polymer, almost rubber, than a metal. A naive explanation would be that this is simply because the elastic deformation region for this metal is unusually large. However, this is not the case at all. In fact, loading and unloading the wire cycles the material between different crystal structures. This is illustrated by a stress vs. strain curve under loading and unloading in Figure 2.2.

As illustrated in Figure 2.2, a typical stress vs. strain diagram can be divided into two regions: elastic and plastic. In the elastic region, the material exhibits a linear response to the applied strain. If the load is released inside this region, the strain is fully recovered. However, once the sample has been stressed beyond its yield point it enters the plastic region. From this

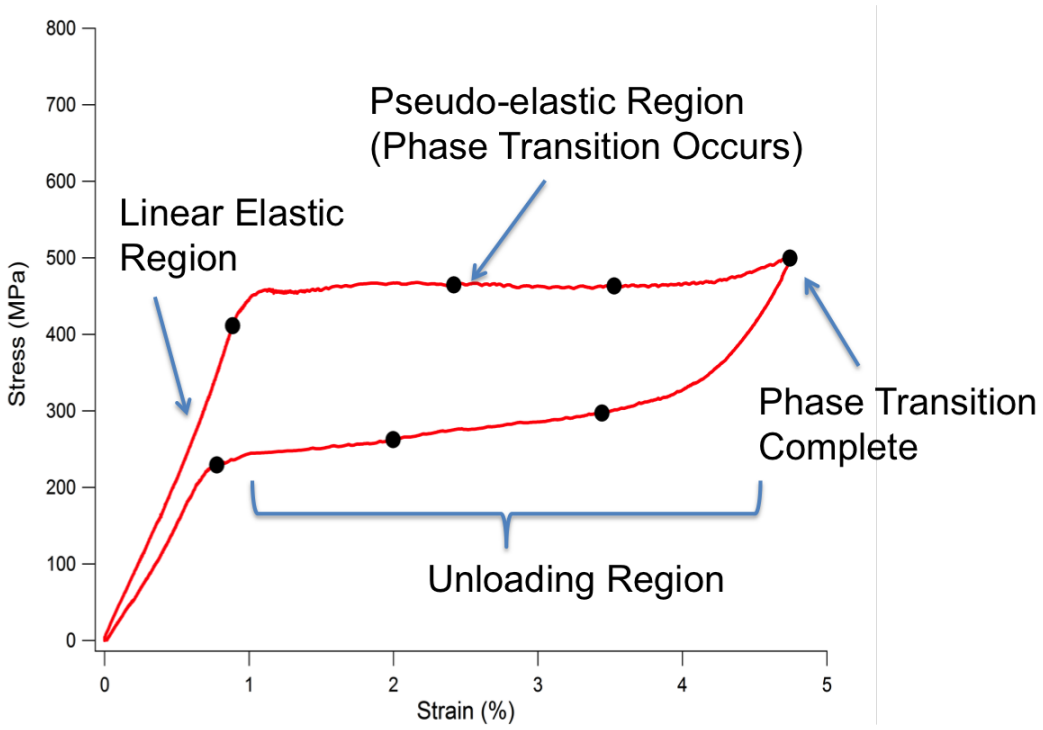

Figure 2.3: Measurement of experimental Stress vs. Strain plot for NiTi under loading and unloading. Measurements performed by Pataky and Sehitoglu [1]

point on, if the load is released, the sample will no longer able to recover the entirety of the strain.

With a pseudoelastic material, a very different behavior is observed. The sample begins with zero load in the high temperature austenite phase. Upon loading, the sample first enters the familiar elastic region until a critical stress is reached. At this point it becomes more energetically favorable for the crystal to transition to the tetragonal martensite phase than to deform by conventional elastic or plastic means. As this phase transformation nucleates, the sample experiences strain at a constant stress until the entire sample is transformed to martensite. At this point, the conventional elastic stress strain behavior resumes, only now for a martensite material. If the sample is unloaded, it will return to an austenite phase and will completely recover all the strain. Since no plastic deformation has occurred, it will return to its undeformed dimensions. In essence, when an SMA undegoes strain, it converts the applied mechanical energy to power a phase transformation rather than break any atomic bonds.

2.2.3 Shape Memory Effect

The most well known property of SMAs is also their namesake, the shape memory effect. This is a process by which a deformed SMA can be returned to its undeformed shape with the application of heat. The exact mechanisms by which different SMAs recover their shape can be quite complex and vary slightly from system to system. However, the driving forces behind the shape memory effect can be explained by the diffusionless nature of the martensitic phase transformation and a process known as detwining. Several different crystal variants of the martensite phase can exist in SMAs. For our purposes we will focus on a modulated or twinned variant and a regular or detwinned variant. The modulated twinned structure forms to accommodate any inherent stress in the material. When a sample of a twinned martensite SMA is subject to strain, rather than breaking any atomic bonds, the sample will detwin. If the sample is heated to above T_{A_F} it will transform to the austenite phase. It can then transform back to martensite through cooling and the previous twinned variant will reform, again accommodating any intrinsic stress. Since all of the processes involved are completely diffusionless, and no bonds are broken, all information about the deformed state that was held in the detwinned structure has been erased. The sample is reset as if it had never been deformed at all. A schematic of this process is shown in Figure 2.4.

2.2.4 The Elastocaloric Effect

If loading and unloading phase transformation cycles are applied to an SMA under adiabatic constraints a change in temperature can be observed. This is known as the elastocaloric effect or ECE. In order to explain the mechanism behind the ECE we will assume a sample of an SMA in the cubic austenite phase that transforms to a tetragonal martensite upon loading. The load is applied under adiabatic constraints until the martensitic phase transformation occurs. Due to the adiabatic constraint, the total entropy of the system is conserved during the transformation such that

$$\begin{aligned} \Delta S_{total} &= 0 \\ \Delta S_{total} &= \Delta S_{thermal} + \Delta S_{structural} \end{aligned} \tag{2.1}$$

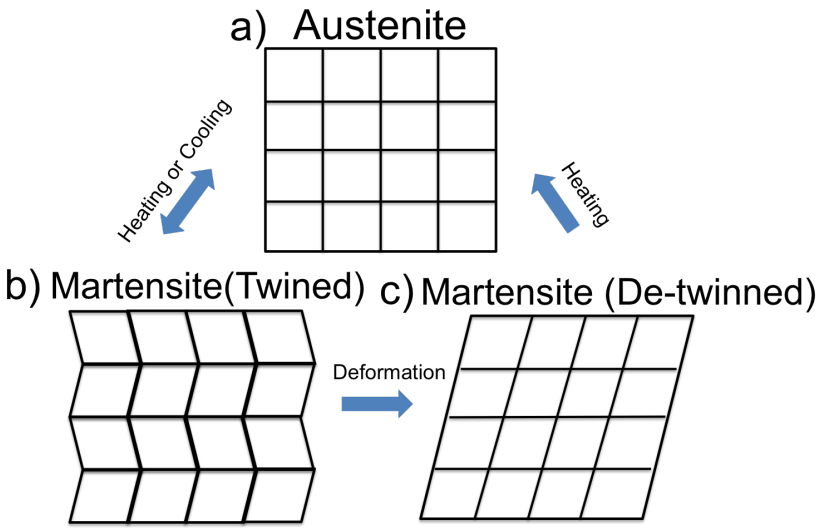

Figure 2.4: The Shape Memory Affect. a) A sample begins as a cubic austenite. b) It is then cooled down to a twinned martensite. c) The sample begins to detwin to accommodate applied loading. a) Upon heating the sample transforms back to a cubic austenite.

where $\Delta S_{thermal}$ is the contribution to the entropy change due to lattice vibrations and $\Delta S_{structural}$ is the contribution as a result of the change in crystal structure.

The transformation from a cubic austenite to a tetragonal martensite represents a decrease in symmetry and thus an increase in the entropy associated with the lattice structure. In order for the total change in entropy, ΔS_{total}, to be conserved, $\Delta S_{thermal}$ must increase. This directly corresponds with an increase in lattice vibrations and thus an increase in temperature. The adiabatic constraint can be removed and the sample temperature is allowed to equilibrate with its surroundings. If the adiabatic constraint is reapplied, and the load is removed, the sample will transform back into an cubic austenite lattice. This decreases $\Delta S_{structural}$ which corresponds to an increase in $\Delta S_{thermal}$ and hence an increase in temperature.

2.2.5 The Magnetocaloric Effect

Assuming a strong enough magnetic field is applied, any magnetic spin disordered or anti-ferromagnetic system can exhibit a magnetocaloric effect. The underlying physics of the magnetocaloric effect are fairly straightforward. An

anti-ferromagnetic or spin disordered system in an adiabatic environment is introduced to a magnetic field. The spins of the system will self align with the field producing an ordered ferromagnetic system. Since the field is introduced in an adiabatic environment, the total entropy of the system is conserved according to the relation

$$\begin{aligned} \Delta S_{total} &= 0 \\ \Delta S_{total} &= \Delta S_{thermal} + \Delta S_{magnetic} \end{aligned} \tag{2.2}$$

where $\Delta S_{thermal}$ is again the contribution to the entropy change due to lattice vibrations and $\Delta S_{magnetic}$ is the change in entropy due to the change in the magnetic order. The alignment of the spins with the magnetic field reduces the entropy contribution due to the spins and thus the contribution from the lattice vibrations must compensate. This leads to an increase in temperature. At this point, the adiabatic constraint can be lifted and the temperature of the sample can equilibrate with the surroundings. Next, the adiabatic constraint is re-applied and the magnetic field is removed. As a result, the spins relax back to their previous anti-ferromagnetic or disordered state, resulting in a decrease of the magnetic contribution to the total entropy. This time, the thermal entropy contribution must decrease in response, resulting in a temperature drop.

2.2.6 Magnetocaloric Effect in Magnetic SMAs

For SMAs that are also magnetic (FSMAs), the ECE and MCE can become coupled. For example, in the magnetic SMA $Ni_{50}Mn_{50-x}In_x$, the cubic austenite phase favors ferromagnetic ordering, while the tetragonal martensite phase favors anti-ferromagnetic ordering. This complicates the behavior of the combined effect. In some cases, such as $Ni_{50}Mn_{50-x}In_x$ FSMAs, this leads to the magnetocaloric temperature change being reversed. The temperature increases when the field is applied and decreases when it is removed. This coupling can also give rise to a larger change in temperature associated with the magnetostructural transformation, sometimes referred to as a giant MCE. One unusual aspect of the MCE in FSMAs is the relative importance of the magnetic order to the stability of austenite and martensite phases. In most materials, the contribution to the total stability of the system is

negligible, however, for FSMAs it is appreciable enough to drive a structural phase transformation.

2.3 A Brief Discussion of Spin Lattice Models

Understanding the phase transformation behavior of any system relies on the ability to find the global minimum of a underlying Hamiltonian. This is often a multidimensional many-body system, making it extremely difficult or more likely impossible to solve analytically. Therefore, a numerical solution is necessary.

In the case of the present work, the framework used to obtain these numerical solutions is a spin lattice model solved via Monte Carlo sampling. In a spin lattice model, the atoms of the crystal system in question are represented as points on a n-dimensional grid. Each point is assigned a set of discrete values which represent the properties of an individual component of the system. The overall state of the system is then described in terms of the interactions between different components as a function of their individual properties. This modeling approach has proven very successful in studying the magnetic properties of materials, most famously in the Ising model, but has also been used in a variety of other fields ranging from economics to biology.

2.3.1 Ising Model and Magnetism

Understanding magnetization in materials is essentially a quantum problem. It arises from the interplay of a particle's spin and the fermionic nature of electrons, protons, and neutrons in an atom. A particle's spin refers to its intrinsic quantized angular momentum, a quantity similar to that of a sphere rotating about an axis. However, as elementary particles are described as waves or point particles it is difficult to envision how they might actually "spin." For the purposes of this document it is convenient to consider these particles as having a radius, when appropriate, so as to avoid too much existential or philosophical distress. If an electron is allowed to have a radius, and since it is a charged particle, this spin results in a magnetic field. The same is true for the nucleus. However, the magnitude of the nuclear moment

is typically significantly smaller than that of the electrons and is usually disregarded. The magnetic moment of a single atom can then be described as the sum of the moments of each of its electrons.

The second key point for discussing the quantum roots of magnetization is that of a fermion. Fermions are a class of particles with half integer spins which satisfy the condition that two otherwise identical particles cannot simultaneously occupy the same state. Therefore, in order for two fermions to occupy the same orbital they must have opposite spins. The electrons in a material must arrange themselves according to this constraint known as an exchange interaction. These exchange interactions can take place through different mechanisms, leading to ordered or disordered arrangements of atomic spins in a lattice, and therefore magnetic or non-magnetic materials.

As with any multi-body problem, analytically determining the magnetic structure of a material quickly becomes intractable. Various assumptions and methods have been developed to deal with this issue. Before the development of tools such as density functional theory (DFT) which can approximate the solution to the many body Schroedinger equation for the system, the magnetic structure of a crystal was solved for by simplifying the system's Hamiltonian into something that was easier to work with. One of the most successful and useful of these is the Ising model. In the Ising model, the system of atoms is divided into a grid with each grid site representing an individual atom. Each atom is then allowed to have a half integer spin, usually $\sigma = \pm\frac{1}{2}$. The total energy of the system is then represented by the effective Hamiltonian:

$$H = -\sum_{i,j} J_{i,j}\sigma_i\sigma_j - \mu\sum_i h_i\sigma_i \quad . \tag{2.3}$$

The first summation is over all sites i and neighboring sites j. It is usually truncated to include only nearest neighbor atoms since the magnitude of magnetic exchange interactions decrease quickly as a function of distance. However, if more complex or longer range interactions need to be accounted for, the summation can be extended to cover any arbitrary set of sites such as triplets or long distance pairs. In the Ising Hamiltonian, $J_{i,j}$ is the interaction coefficient between atoms i, j based on their spins. The second summation is added to allow for the inclusion of an external magnetic field

h, and magnetic moment μ. When framed in this way, the problem of evaluating and minimizing the effective Hamiltonian can be easily approached computationally.

The Ising model is one of the most basic models for describing spin interactions between atoms in a lattice. However, it can still yield important insights and surprisingly accurate results when applied correctly to problems of magnetism and magnetic phase transformations. For the particular case where $J_{i,j} = J'$ some important behaviors can be observed without having to explicitly solve for the Hamiltonian minimum. A simple analysis will show that if J' is positive, the lowest energy configuration would arise from an antiferromagnetic arrangement of spins. Conversely, if J' is negative, the lowest energy configuration would arise form a ferromagnetic arrangement of spins. This is a relatively good model for describing the exchange interactions in materials that follow the Heisenberg model of magnetism.

The energy and average magnetization for any arrangement of spins on a lattice can be easily evaluated by summing over all lattice sites. However, since this model is describing a natural phenomenon, it is useful to consider the "solution" to the Ising model as the configuration that minimizes the Hamiltonian. In order to gain information about the ground state configuration, or how such a system will evolve as a function of temperature, additional methods, such as Monte Carlo strategies, are often implemented.

2.3.2 Blume-Emery-Griffiths Model and Martensitic Phase Transformations

Different effective Hamiltonians have been developed to study various phenomena. In the case of martensitic phase transformations, one of the more successful models has been the Blume-Emery-Griffiths model (BEG). The Blume-Emery-Griffiths model was originally designed to study first-order phase transformations and phase separation in liquid He^3-He^4 mixtures and takes the form:

$$\mathcal{H} = -J \sum_{i,j} \sigma_i \sigma_j - K \sum_{i,j} {\sigma_i}^2 {\sigma_j}^2 + \Delta \sum_i {\sigma_i}^2 \quad . \tag{2.4}$$

Here the summations are over all points i and neighbors j on an n-dimensional lattice [13]. The original BEG model was later revised by Vives, Castán, Lindgård and Burkhardt to create the degenerate BEG (DBEG) model and applied to the study of first order martensitic phase transformations [14, 15, 16]. In the DBEG model, the crystal field Δ is shifted by a degeneracy parameter $k_B T \ln(p)$, where k_B is the Boltzmann constant and p is an integer representing the system degeneracy. For the case where $\Delta = zK$, where z is the coordination number, the DBEG hamiltonian takes the form:

$$\mathcal{H} = -\sum_{i,j}(J_{ij}\sigma_i\sigma_j - K_{ij}(1-{\sigma_i}^2)(1-{\sigma_j}^2)) - k_b T\ln(p)\sum_i(1-{\sigma_i}^2) \quad (2.5)$$

The σ term represents the atomic displacement of a site in a cubic austenite lattice and can take values of $\pm 1, 0$. A σ of zero represents an austenite lattice site site with zero strain. However if some arbitrary strain were to be introduced the site could be deformed into one of six degenerate variants, corresponding to displacements in the $\pm x, y, z$ directions and assigned corresponding values of ± 1. Assuming that the strain is uniaxial, the system can be simplified to contain only two variants. The J_{ij} and K_{ij} are the interaction coefficients for martensite and austenite respectively. In the case of a martensitic phase transformation, these coefficients do have a physical significance related to the phonon modes of the crystal. However for our purpose it is more helpful to consider J_{ij} and $K_{ij}$the contributions to the system stability from martensite or austenite lattice sites. This is easily illustrated with a brief analysis if we assume that the system in question is entirely made up of a single phase or phase variant.

In the low temperature purely martensitic case (where all sites have $\sigma_n = +1$ or $\sigma_n = -1$) the Hamiltonian simplifies to

$$\mathcal{H} = -\sum_{i,j}(J\sigma_i\sigma_j) = -\sum_{i,j} J \quad (2.6)$$

We can then consider the J term to be the contribution to the Hamiltonian of a martensitic system. Similarly, we can show that if we have an austenitic lattice, our Hamiltonian will simplify to

$$\mathcal{H} = -\sum_{i,j}(K(1-{\sigma_i}^2)(1-{\sigma_j}^2)) = -\sum_{i,j} K \quad (2.7)$$

and K can be interpreted as the contribution from austenitic systems.

2.3.3 Metropolis Monte Carlo

As mentioned in a previous section, the ground state configuration of a spin lattice model can be found by finding the configuration that minimizes the energy of the Hamiltonian. One of the most common algorithms for this application is the Metropolis Monte Carlo method. The algorithm itself is quite simple. In Metropolis Monte Carlo the population of states in the system is assumed to follow a Boltzmann distribution

$$F_{state} \propto e^{-\frac{E}{k_B T}} \tag{2.8}$$

where E is the system energy, k_B is the Boltzmann constant, and T is the system temperature. The following algorithm is then used to minimize the system energy:

- A site is selected at random. The state is recorded and the energy is calculated from the Hamiltonian.
- The state of the site is changed, and the energy is re-evaluated.
- Energies are compared before and after the change.
  - The change is accepted if the energy decreases after the change.
  - If the energy increases after the change it is accepted with probability P_{accept}, which is defined as:

$$P_{accept} = e^{-\frac{\Delta E}{k_B T}} \tag{2.9}$$

Using this algorithm, it can be shown that the ground state can be found for any system given an infinite number of iterations. However, in finite practical application this algorithm can find local minimums and become stuck. This problem is known as critical slowing down, and alternative algorithms have been developed to overcome this limitation.

CHAPTER 3

LITERATURE REVIEW

The idea of using the MCE for refrigeration first appeared in the 1920s and was successfully utilized in the 1930s for experiments at cryogenic temperatures [5]. It wasn't until the turn of the century that any device capable of operating at room temperature was developed. However, this device required the expensive element gadolinium, making it an unattractive alternative to vapor compression systems [5]. While a number of other promising candidate materials have been proposed, many require either rare and expensive elements or environmentally harmful compounds. The absence of these particular drawbacks has driven the research community to consider Ni-Mn based Heusler alloys as promising alternatives. In general Heusler alloys follow the formula $X_{50}Y_{25}Z_{25}$, where X and Y are transition metals and Z is usually a group III, IV, or V element [5, 7]. An example of the typical martensite and austenite crystal structures are shown in Figure 3.1. Certain Ni-Mn based alloys have been well studied experimentally. Of particular interest to this document are the works of Ito *et al.* [17] and Liu *et al.* [6] which focus on $Ni_{50}Mn_{50-x}$Inx alloys. Ito *et al.* did extensive work determining properties important for MCE performance for a significant range of $Ni_{50}Mn_{50-x}In_x$ compositions, which, as discussed in Chapter 4, is extremely useful for benchmarking computational frameworks for these alloys. The importance of these materials was highlighted by Liu *et al.*, who recorded a change in temperature of up to -6.2K under a 2T magnetic field for cobalt doped Ni-Mn-In alloys.

Despite their promise, these materials come with their own set of challenges, such as significant hysteresis effects and variability of MCE performance with small changes in alloy composition [2, 5]. This complexity is illustrated in Figure 3.2, where the martensitic transformation temperature changes by 600K over a ten percent chance in nickel composition [2]. The sensitivity of key material properties for MCE effectiveness makes exper-

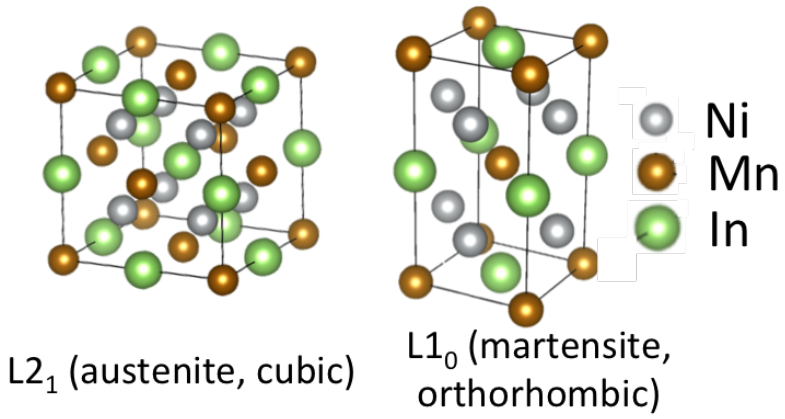

Figure 3.1: Example of cubic austenite and tetragonal martensite phases of the Heusler alloy Ni_2MnIn. While this precises composition does not exhibit a MCE, off stoichiometric compositions do.

imental surveys of the entire phase space a prohibitively time-consuming process. Therefore any computational tool for predicting the magnetocaloric performance is a valuable asset. Early work in this field was carried out by Vives, Castán, and Lindgård in 1999 [18]. Their approach consisted of a combination of a degenerate Blume-Emery-Griffiths model (DBEG) and an Ising model, with a coupling component to capture the magnetostatic phase transformation in Ni_2MnGa. This work was expanded on by Buchelnikov, Entel, Taskaev Sokolovskiy *et al* (BETS). They replaced the Ising model with a q state Potts model, to better capture the first-order nature of the phase transformation. Additionally, the Potts model and portions of the coupling component of the model were parametrized directly from *ab-initio* simulations. The BETS model has been used to simulate the magnetostructural transformation in various Ni-Mn-X alloys such as X=(Ga, In, Sn, Sb) [2, 5, 19] as well as to study the effects of dopants such as Co, Cu and Cr on the MCE (Figure 3.3) [20, 21, 22]. It has also been used in a predictive capacity to help develop design rules for the minimization of hysteresis in Ni-Mn based Heuslers [3, 10]. The BETS model has proven useful as both a descriptive and predictive tool. However, its reliance on experimental data for some of its key parameters diminishes its effectiveness as a tool for materials discovery.

From a materials discovery perspective it would be useful to have a tool that could function without the need for previous experimental data. In the

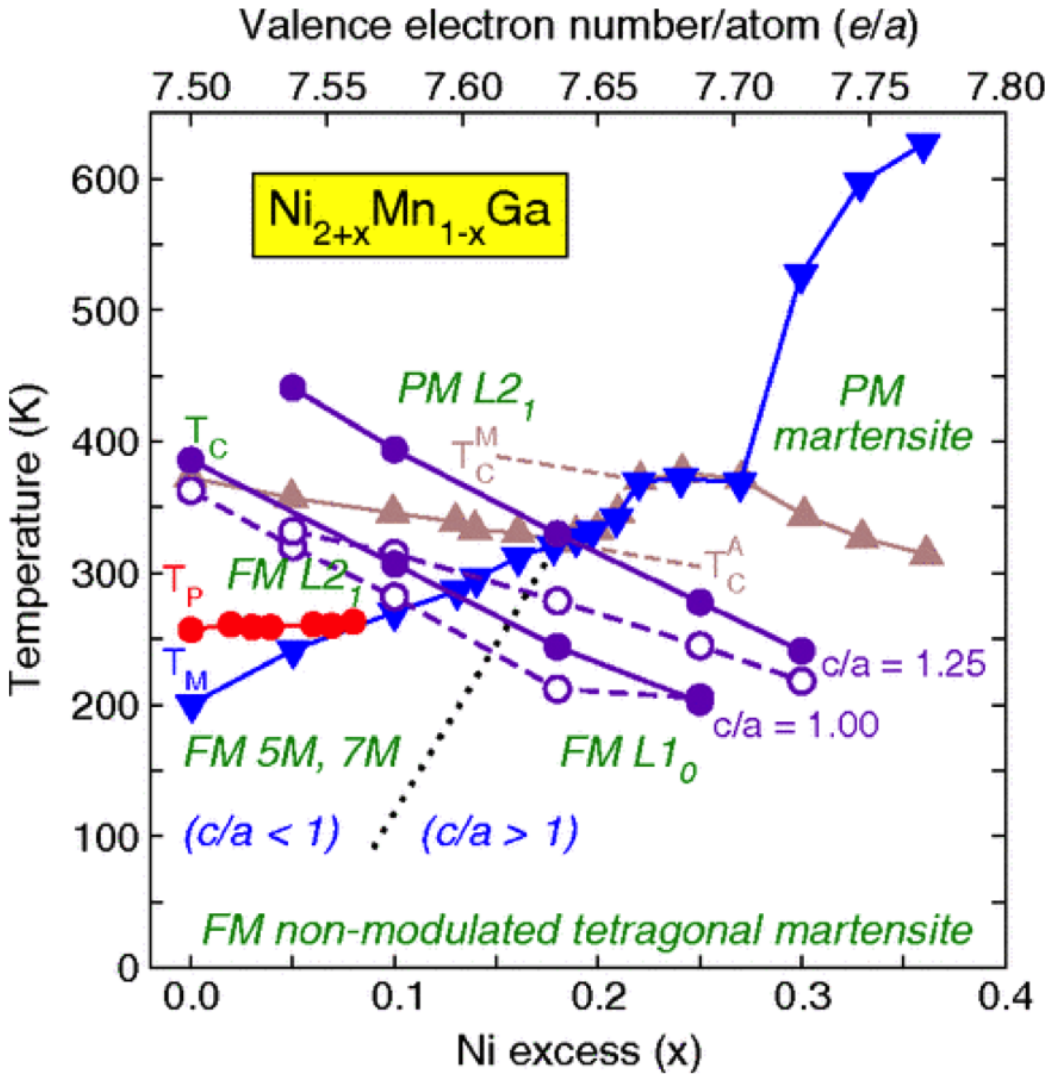

Figure 3.2: Phase diagram of $Ni_{2+x}Mn_{1-x}Ga$. The blue line represents the martensitic transformation temperature, the red line marks the paramagnetic transition temperature, the purple lines represent the Curie temperatures predicted through Monte Carlo simulations, and the tan line represents the extrapolated magnetic transformation temperature. Several distinct regions with separate crystal variants, phase and magnetic structures are present over a small section of the phase space [2].

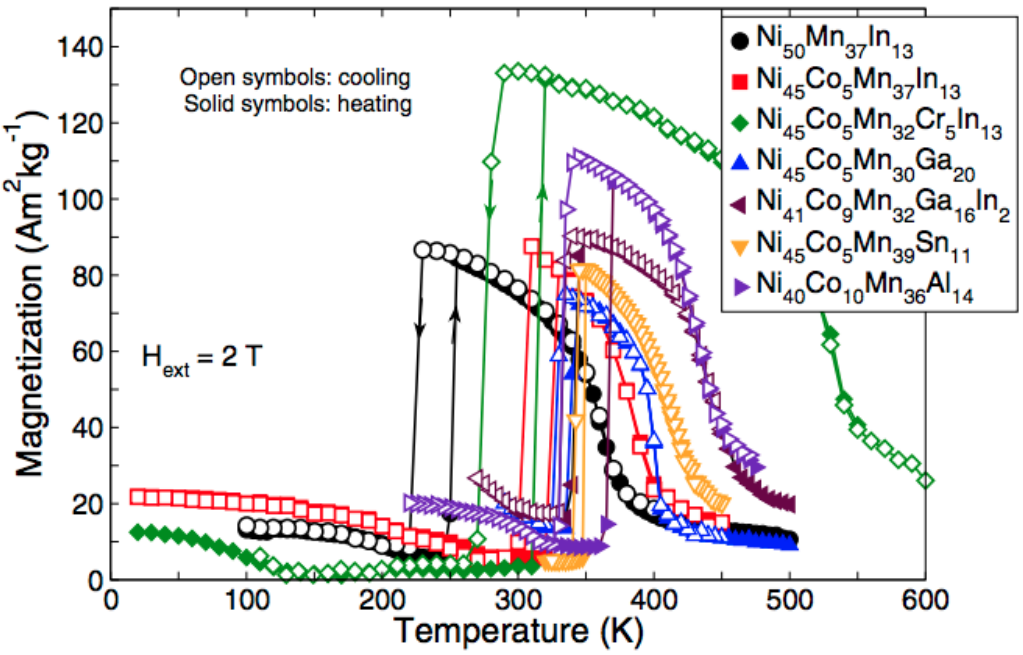

Figure 3.3: Magnetization vs. temperature curves in a constant magnetic field of 2 Tesla for doped and undoped Ni-Mn based alloys. The curves represent heating and cooling cycles with closed symbols indicating heating and open symbols indicating cooling. Varying degrees of hysteresis are observed for all alloys [3].

remainder of this document, we introduce a new model for predicting the properties of FSMAs across a materials composition space. Using a degenerate Blume-Emery-Griffiths model (DBEG) and Monte Carlo sampling techniques we can examine a material's behavior across magnetic and structural phase transformations. The model is parametrized solely from first principles data and a single tuning parameter. Unlike the previous works discussed, our method relies on dynamic DBEG parameters that are dependent on the local environment. Preliminary results from simulations of $Ni_{50}Mn_{50-x}In_x$ have shown transition temperatures that appear to be in good agreement with experimental results.

CHAPTER 4

COMPUTATIONAL FRAMEWORK AND MODEL FITTING RESULTS

In order to design a model of any system, it is necessary to first acquire a general understanding of the laws that govern the system. In our case, this entails acquiring an understanding of the physics that governs FSMAs. The FSMAs used to develop the model were $Ni_{50}Mn_{50-x}In_x$. These alloys have phase transformations from tetragonal low-temperature phases to cubic high-temperature phases and have been well-documented experimentally [17, 23]. In addition to structural phase transformations $Ni_{50}Mn_{50-x}In_x$ undergoes a magnetic phase transformation from a low temperature ordered, antiferromagnetic structure to a higher temperature ferromagnet before it becomes spin disordered at its Curie temperature. The structural and magnetic transformations are both dependent on the precise composition of the alloy.

4.1 Magnetic Structure of $Ni_{50}Mn_{50-x}In_x$

In an effort to understand the nature of this dependence and the coupling between the structural and magnetic contributions, a number of different DFT simulations were carried out. To determine the initial lattice parameters, a 16 atom tetragonal cell of $Ni_{50}Mn_{50-x}In_x$ with a composition of $x = 25$ was relaxed and then distorted along the tetragonal axis with different ratios of lattice constants. The results, shown in Figure 4.1, clearly show the existence of two stable local minima and one unstable equilibrium. The most stable minimum represents the tetragonal martensite structure while the other likely indicates the existence of a modulated variant which, for the purpose of the model, is disregarded. The unstable equilibrium represents the cubic austenite structure which will become more stable at higher temperatures.

In order to analyze the magnetic structure, three points were chosen from

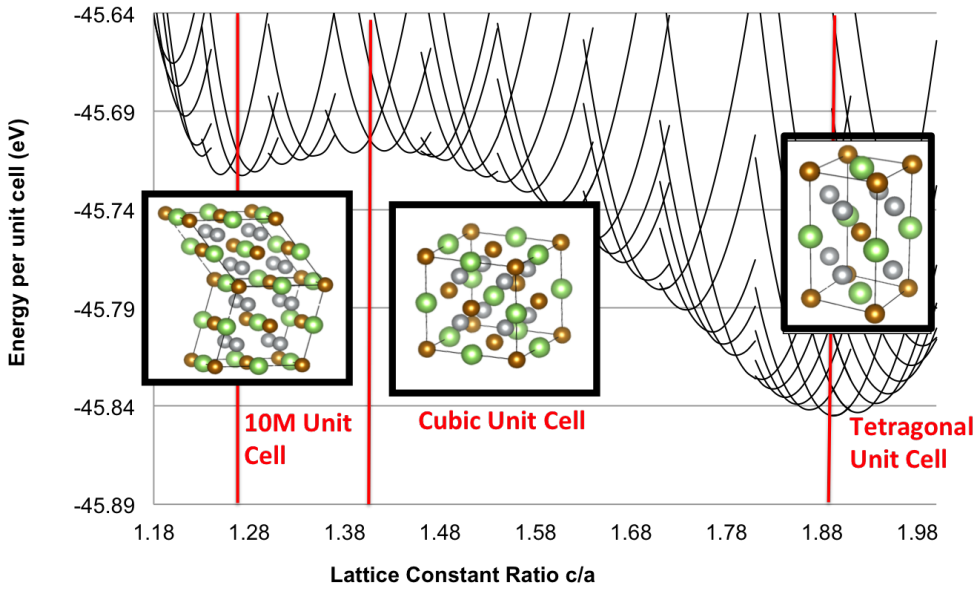

Figure 4.1: Ground state energy landscape for $Ni_{50}Mn_{25}In_{25}$. Each individual paraboloid represents a constant lattice volume with a changing ration of lattice constants c/a. The experimentally observed tetragonal and cubic phases are marked, as well as a third phase with lattice constants similar to those expected of a modulated martensite phase if such distortions had been allowed in the calculations.

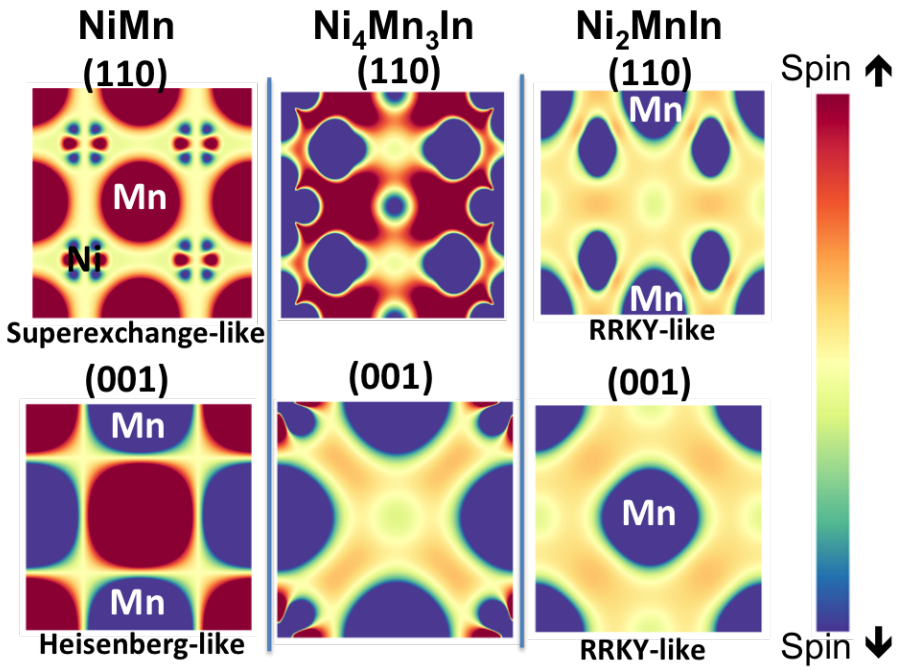

Figure 4.2: Spin density plots for $Ni_{50}Mn_{50-x}In_x$ with x=0, x=12.5 and x=25. The top row shows the density in the [110] crystal plane and bottom row shows the density in the [001] plane. The first two columns depict a tetragonal ground state structure while the third depicts a cubic ground state.

the $Ni_{50}Mn_{50-x}In_x$ phase space: x=0, x=12.5 and x=25. For each of these compositions, a 16 atom cell was constructed for a martensite and austenite phase. A separate calculation was carried out for every possible arrangement of spins and atomic positions in a standard cubic or tetragonal cell. Both phases can be described in terms of two intersecting simple cubic or tetragonal sub-lattices. One sub-lattice is made up for Ni sites and the other of Mn-In sites. When generating possible configurations for atomic positions, each atomic species was confined to its respective sub-lattice. All calculations were performed with the DFT software package VASP [24, 25, 26, 27] and projector augmented-wave PBE potentials [28, 29]. A standard k-point mesh of 7x7x7 and energy cutoff of 500eV were used.

The spin density plots for each structure were examined to gain intuition for the nature of the magnetic interactions present at each composition. Of particular interest were the structures that had the lowest overall energy since they would be the most stable and most likely to be observed in nature. For each of the three compositions chosen, the lowest energy austenite

and martensite structures are shown in Figure 4.2 as spin density plots. While these are only a small sample of all the spin configurations generated, they highlight how the magnetic interactions change as a function of indium concentration.

In systems with no indium, the ground state structure is tetragonal. The manganese atoms have the largest spin moment and align themselves antiferromagnetically in the [001] plane and ferromagnetically along the tetragonal axis. From the spin density plots, it appears that the anti-ferromagnetic exchange in the [001] plane is similar to Heisenberg magnetism, while in the [110] plane there appear to be longer-range interactions similar to superexchange between the manganese and nickel atoms. As the indium concentration is increased, the antiferromagnetic structure is interrupted by the low spin indium atoms and a large number of similarly stable spin arrangements can be formed. At this concentration, identifying the nature of the exchange interactions becomes more difficult and no further speculation can be made. Once the indium concentration is sufficiently increased and the short range Mn-Mn interactions have been replaced, the ground state structure becomes cubic. This in turn is accompanied by a ferromagnetic spin arrangement. In this case, the spin density plots seem to reflect a form of magnetic exchange similar to RKKY interactions, with the nickel and manganese spins interacting ferromagnetically, mediated by antiferromagnetic interactions with delocalized conduction electrons. This progression from tetragonal, antiferromagnetic, low-indium concentration to cubic, ferromagnetic, high-indium concentration must be born out in any model concerned with the effects of alloy composition on the magnetocaloric effect in $Ni_{50}Mn_{50-x}In_x$.

4.2 Model Design

The method we chose for modeling the behavior of FSMAs relies heavily on the DBEG, discussed in Chapter two and displayed again for convenience:

$$\mathcal{H} = -\sum_{i,j}(J\sigma_i\sigma_j - K(1-{\sigma_i}^2)(1-{\sigma_j}^2)) - k_BT\ln(p)\sum_i(1-{\sigma_i}^2) \quad . \quad (4.1)$$

While the DBEG is well-suited for describing the structural phase transformation, it does not inherently have any mechanisms to incorporate the

coupling of the magnetic and lattice structure or changes in stoichiometry that are important in describing the physics of FSMAs. In order to accommodate these factors, we create an effective Hamiltonian that replaces J and K with dynamic parameters. In this new form, J and K are evaluated at each lattice point and are functions of the spin and atomic species of that point and its neighbors. The effective Hamiltonian can be written as follows:

$$\mathcal{H} = -\sum_{i,j}(J_i'\sigma_i\sigma_j - K_i'(1-{\sigma_i}^2)(1-{\sigma_j}^2)) - k_BT\ln(p)\sum_i(1-{\sigma_i}^2) \quad (4.2)$$

where J' and K' are the dynamic parameters. These parameters are calculated as linear combinations of a cluster expansion over the spins of neighboring atoms and a cluster expansion over the species of neighboring atoms.

$$J_i' = \sum_{clusters\ j} M_j s_i s_j + \sum_{clusters\ j} N_j \quad (4.3)$$

$$K_i' = \sum_{clusters\ j} P_j s_i s_j + \sum_{clusters\ j} Q_j \quad (4.4)$$

where s_n represents the spin of a particular site and can take values $\pm 1, 0$. The parameters M, N, P, Q are vectors of length equal to the number of clusters used, and are fit from first-principles data. The resulting composite model can then be solved using several different Monte Carlo techniques.

4.3 Fitting Model Parameters

The parameters for the cluster expansions were fit from a DFT dataset consisting of structures that span the phase space of the material in question. Three specific compositions were chosen for the $Ni_{50}Mn_{50-x}In_x$ alloy, $x = 0, 12.5, 25$. At each of these compositions, supercells were generated that represent every unique population of spins and species allowed within a 16 atom supercell. This process was repeated for both austenite and martensite.

In order to fit the N, M, P and Q vectors from the DFT data, it is first necessary to define the clusters to be used for the spin and composition cluster expansions. After examining spin density plots from the DFT data, it appeared that both long-range and short-range spin interactions play important roles in determining the magnetic structure. Therefore first, second and

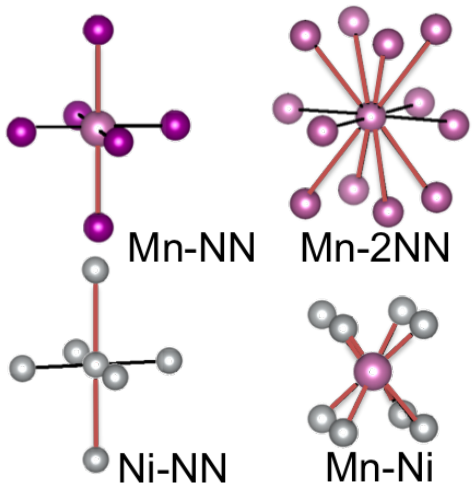

Figure 4.3: Examples of clusters used to account for spin and local composition. The red lines connecting certain atoms represent pairs that lie along the axis of tetragonal distortion. These pairs are fit separately from those that lie in the plain orthogonal to the tetragonal axis.

third nearest-neighbor pairs were included in the expansion for the magnetic contributions. In order to simplify the fitting process, the neighbor distances between atoms was defined in terms of the cubic austenite unit cell. A distinction is made between neighbor pairs along the direction of the tetragonal distortion in order to account for relative changes in distance following the phase transformation. For the clusters based purely on the local composition, it was determined that the minimum number of clusters should include interactions between each of the atomic species. This was accomplished using second nearest-neighbor interactions for Ni-Ni, Mn-Mn, Mn-In and In-In as well as first nearest-neighbor interactions for In-In. The interactions for Ni-Mn and Ni-In were discarded since they proved to be redundant. Monomer terms were also included. Examples of some of the clusters used are shown in Figure 4.3.

Austenite and martensite instances were created for each cluster, with the austenite clusters used to calculate K' and the martensite clusters used to calculate J'. In total, 23 spin clusters and 42 composition clusters were chosen. Of these clusters, some showed zero contribution to the total Hamiltonian upon summing and were disregarded.

In order to prepare the data for the fit, the VASP output for each system

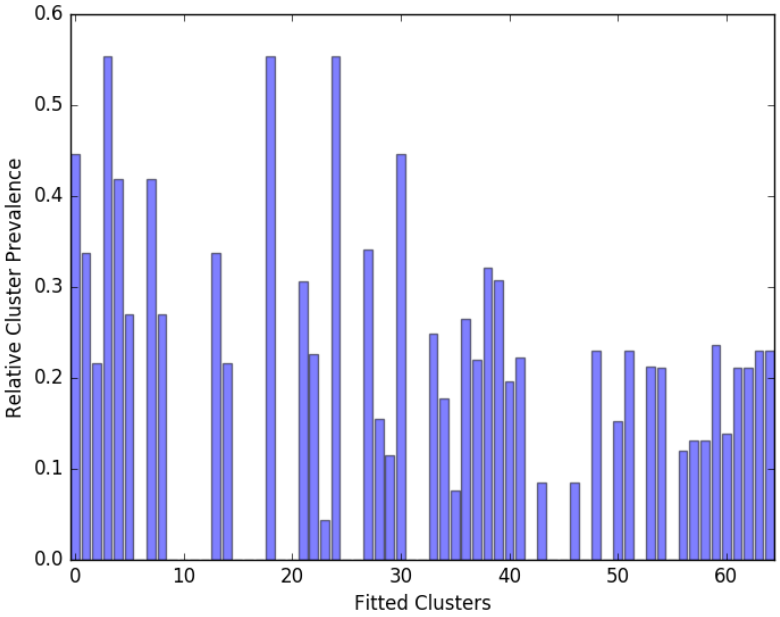

Figure 4.4: Relative prevalence of each cluster type in the dataset. The y-axis represents the ratio of total possible occurrences of a cluster to actual instances in the data set.

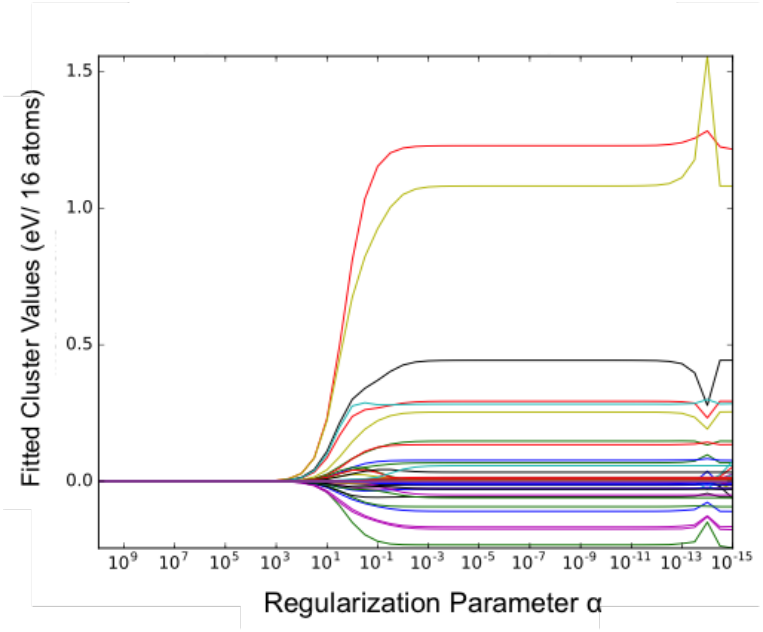

Figure 4.5: Fitted clusters from ridge regression as a function of regularization parameter α. The optimum value of α was determined to be the order of 10^{-2}.

is scanned for relevant information. This includes the magnetic moment, species, and position of each atom, as well as the total energy for each system. This information is then processed to determine the number of occurrences of each cluster for an individual system. As previously mentioned, some of the proposed clusters never occurred in any of the systems in the data set. These are filtered out and the set of clusters is revised. This is illustrated in Figure 4.4. The remaining 44 cluster expansion parameters are then fit using ridge regression and cross validation to determine the regularization parameter α. The optimal α was determined to be the one that converged the cross validation score R^2 to 1. Here R^2 is calculated as

$$R^2 = (1 - \frac{u}{v}) \tag{4.5}$$

where u is the residual sum of squares and v is the total sum of squares. The values of the clusters as a function of α are shown in Figure 4.5.

A comparison between the total energy predicted from DFT and total energy predicted by the fitted model is shown in Figure 4.6. From this figure we can see that the fitted model correctly identifies the lowest energy struc-

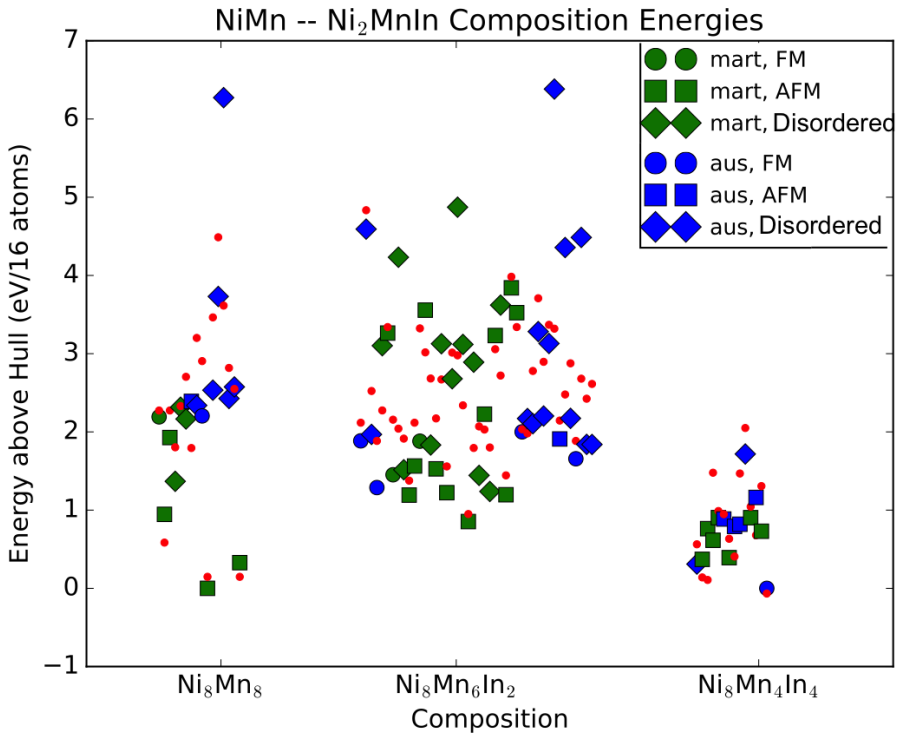

Figure 4.6: Comparison of total energy predicted in DFT to total energy calculated using the fitted cluster parameters. Red symbols indicate calculated energies from the fitted cluster parameters. The x-axis is divided into three sections, one for each composition. For each of the sections, the data points are spread out to make the plot easier to read.

tures for each of the three composition. This is of primary importance for the model since the lowest energy structures are what should be observed in nature. The fitted points also appear to bear out the trend that at low temperatures structures with low indium concentration should favor tetragonal anti-ferromagnetic structures. As the indium concentration increases, different magnetic structures become similarly stable and cubic austenite structures begin to become competitive. Finally, once the indium concentration reaches a critical point the cubic ferromagnetic structures become the most stable.

4.3.1 Monte Carlo Methods

While DFT is a powerful computational tool, it is limited to describing structures at zero temperature. Therefore, Monte Carlo methods can be implemented as a means of extending the predictive power to the temperatures needed to describe the phase transitions that give rise to the MCE. For the Monte Carlo portion of the model a 3D lattice is generated, representing a $Ni_{50}Mn_{50-x}In_x$ supercell. Each lattice site holds three values: phase, species and spin. These in turn correspond to the DBEG and species cluster and the spin cluster components of the model.

Initially the Metropolis algorithm was used for spin, species and phase. However critical slowing down was observed around the phase transformation, necessitating the implementation of a different algorithm. The algorithm used is a combination of Metropolis, Wolff and mixed cluster approaches.

In the first step of our approach, a standard Metropolis algorithm is used to sweep over the lattice and attempt to change the spin of a site or swap the species of a pair of sites. For the species attempts, the pairs are chosen at random under the constraint that they represent Mn-In swaps. This maintains the correct stoichiometry throughout the simulation and reduces the runtime of the algorithm. Before each individual spin or species flip, the J' and K' parameters are recalculated to ensure that the acceptance probability of each move, calculated from the effective Hamiltonian, reflects the current local environment.

In order to avoid problems with critical slowing down, a cluster moves method is implemented for the DBEG component. We choose to implement a combination of a Wolff algorithm with mixed cluster moves first proposed by Bouabci and Carneiro [30]. In this method, a site is chosen at random with a phase σ_c, and a change in phase σ_p is proposed. Depending on the values of σ_c and σ_p one of three procedures is used. If $\sigma_c = \pm 1$ and $\sigma_p = \mp 1$ then the standard Wolff algorithm is used. Otherwise, clusters of sites are grown that contain a mix of either $\sigma = -1, 0$ or $\sigma = 1, 0$. If $\sigma_c = 1$ and $\sigma_p = 0$ or $\sigma_c = 0$ and $\sigma_p = -1$ a cluster of sites is grown with allowed values of $\sigma = 1, 0$. If $\sigma_c = -1$ and $\sigma_p = 0$ or $\sigma_c = 0$ and $\sigma_p = 1$ a cluster of sites is grown with allowed values of $\sigma = -1, 0$. Sites are added to the cluster with a probability of $P_{eq} = 1 - exp(-J' - K'/3)$ if the site being added

has the same phase as the last site added to the cluster, and a probability of $P_{diff} = 1 - \exp -J' + K'/3$ if the sites have different phases. Once the growth of the cluster has stopped, the entire cluster is flipped. In clusters that contain $\sigma = 1, 0$ sites that are $\sigma = 1$ are changed to 0 and $\sigma = 0$ to -1. In clusters that contain $\sigma = -1, 0$, sites that are $\sigma = 0$ are changed to 0 and $\sigma = 0$ to 1. In reference [30], the flip is always accepted if it results in a decrease in the Hamiltonian, or with a probability of $P_{accept} = e^{-\frac{\Delta E}{k_B T}}$ if it results in an increase. However, at this point, our implementation and that of reference [30] differ. Once the cluster is grown and the flips are made, a separate set of Metropolis passes are made over the cluster attempting to flip the site spins. Once a set number of Metropolis passes have been completed, the same acceptance procedure is used as in reference [30]. It is important to note that this method can still exhibit problems due to metastability for certain ratios of K/J. However, for our purposes this has not proven to be an issue [31].

The three Monte Carlo simulations - spin, species and phase - are run sequentially. However, as noted earlier, the spin and composition components of the model depend on the phase. Therefore after each move of the DBEG component it is necessary to allow time for the spin and composition components to equilibrate. Experimenting with relaxation times has shown that only around twenty spin moves and twenty species moves are needed, ensuring that the model runtime remains manageable.

CHAPTER 5

MONTE CARLO RESULTS

The methods discussed in previous sections have been implemented in an open source python code. At this point, it has only been used for benchmarking tests for systems of 128 atoms and 100 Metropolis passes through the lattice for spin and species, and 100 cluster growth attempts for a given simulation temperature. This is due to the large amount of time it takes for the simulation to run. Figure 5.1 shows the phase vs. temperature for a simulation of $Ni_{64}Mn_{48}In_{16}$ (or 12.5% In), while Figure 5.2 shows the average magnetization vs. temperature data for the same alloy.

The predicted T_{M_S} and T_{M_F} appear to be around 300K and 250K respectively. The transition temperatures for alloys with 13% In have been shown experimentally to be $T_{M_S} = 387$ and $T_{M_F} = 386$ [17]. Our results from Monte Carlo are much closer to the experimental values for alloys with 15% In of $T_{M_S} = 297K$ and $T_{M_F} = 283K$ [17]. In fact, as seen in Figure 5.2, the overall behavior of the magnetization vs. temperature curve follows a similar trend to that of the experimental curve from reference [17] with 15.5% In.

Despite the lack of precise agreement with experiment, from the standpoint of a tool for materials discovery, it is much more important to have the general trend correct than to have a precise agreement with experimental values. Additionally, longer simulation times and larger simulation sizes may tighten the difference in the transformation temperatures and give a clearer picture of the magnetization vs. temperature behavior.

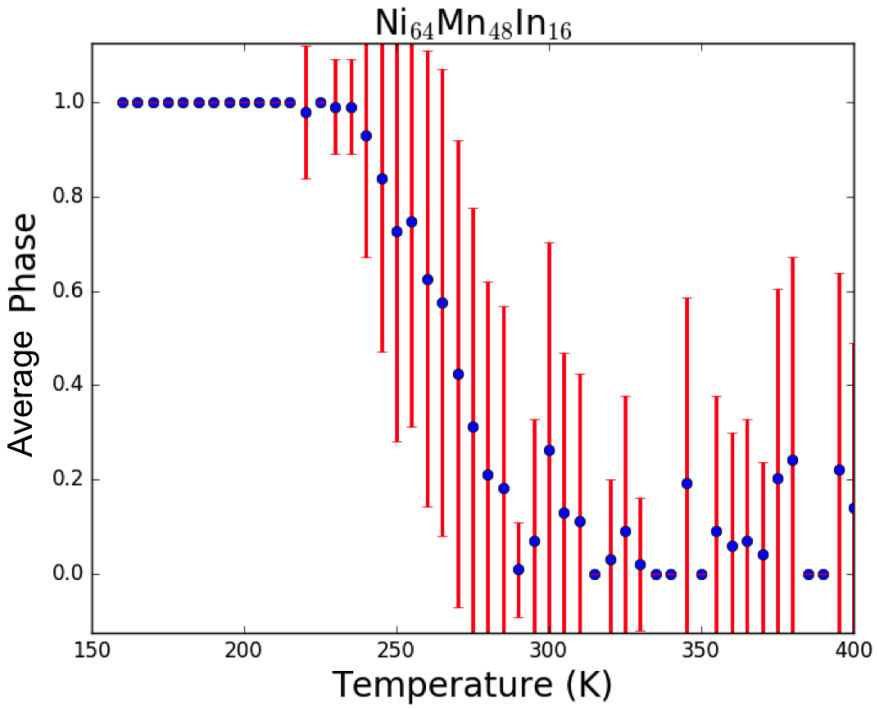

Figure 5.1: Average phase vs. temperature for $Ni_{64}Mn_{48}In_{16}$. The simulation represents cooling from 400K to 150K.

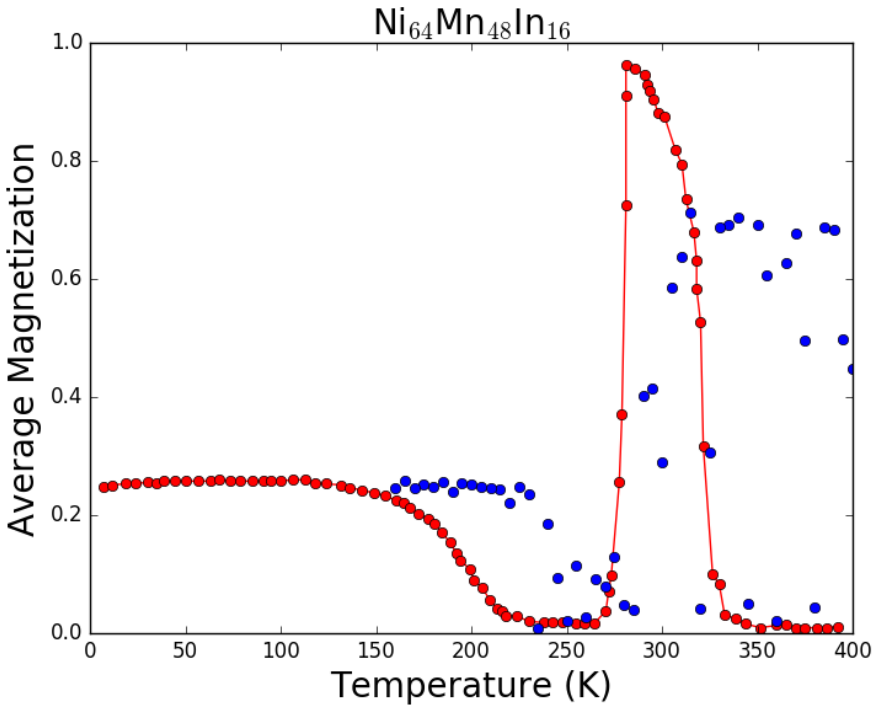

Figure 5.2: Absolute value of average magnetization vs. temperature for simulated $Ni_{64}Mn_{48}In_{16}$ (blue) and experimental values for $Ni_{50}Mn_{35}In_{15}$ (red) [4]. Values obtained from simulation have been normalized for better comparison with experiment.

CHAPTER 6

FUTURE WORK

The final goal of this research is to develop an open source platform capable of a high throughput search for Heusler alloys that exhibit the MCE, as well as to determine the optimal composition of alloys for the MCE. In order to further this goal, work is needed to increase the speed of the algorithm and perform benchmark tests. In order to decrease the error in the Monte Carlo simulation, an order of magnitude increase in the number of Metropolis and Cluster moves will be required. The resulting increase in runtime will diminish the effectiveness of the model as a high throughput tool. In order to diminish the increase in runtime, two separate steps will be taken. First, the current python implementation of the model will be replaced by a faster C++ version. Secondly, if the speedup is still insufficient, the model will be parallelized. These two steps will enable the model to generate more accurate results with larger simulation sizes.

In order for the the model to be a useful tool for materials discovery, it is important that it be able to accurately reproduce trends seen in experiment. To this end, tests will be carried out on different $Ni_{50}Mn_{50-x}In_x$ alloys to examine the change in predicted properties with small changes in composition. Properties of interest will include starting and finishing transition temperatures, Curie temperature, hysteresis width and changes in entropy.

An additional question that could be addressed using the methods discussed in this document is the effect of lattice order and disorder on the MCE. This has been shown to contribute to MCE effectiveness [32]. Disorder effects could be studied by freezing the atomic positions of systems with short-range and long-range order, and for completely disordered systems. This will require simulations with considerably more than the 128 atoms currently used. Therefore, it will require the higher speeds of the C++ and parallel implementations.

REFERENCES

[1] G. J. Pataky, E. Ertekin, and H. Sehitoglu, "Elastocaloric cooling potential of NiTi, Ni2FeGa, and CoNiAl," *Acta Materialia*, vol. 96, pp. 420–427, sep 2015. [Online]. Available: https://www.sciencedirect.com/science/article/pii/S1359645415003948

[2] V. D. Buchelnikov, V. V. Sokolovskiy, H. C. Herper, H. Ebert, M. E. Gruner, S. V. Taskaev, V. V. Khovaylo, A. Hucht, A. Dannenberg, M. Ogura, H. Akai, M. Acet, and P. Entel, "First-principles and Monte Carlo study of magnetostructural transition and magnetocaloric properties of Ni 2 + x Mn 1 x Ga," *Physical Review B*, vol. 81, no. 9, p. 094411, mar 2010. [Online]. Available: https://link.aps.org/doi/10.1103/PhysRevB.81.094411

[3] P. Entel, M. E. Gruner, S. Fähler, M. Acet, A. Çahr, R. Arróyave, S. Sahoo, T. C. Duong, A. Talapatra, L. Sandratskii, S. Mankowsky, T. Gottschall, O. Gutfleisch, P. Lázpita, V. A. Chernenko, J. M. Barandiaran, V. V. Sokolovskiy, and V. D. Buchelnikov, "Probing Structural and Magnetic Instabilities and Hysteresis in Heuslers by Density Functional Theory Calculations," *physica status solidi (b)*, vol. 255, no. 2, p. 1700296, feb 2018. [Online]. Available: http://doi.wiley.com/10.1002/pssb.201700296

[4] A. K. Pathak, M. Khan, I. Dubenko, S. Stadler, and N. Ali, "Large magnetic entropy change in Ni50Mn50xInx Heusler alloys," *Applied Physics Letters*, vol. 90, no. 26, p. 262504, jun 2007. [Online]. Available: http://aip.scitation.org/doi/10.1063/1.2752720

[5] V. D. Buchelnikov and V. V. Sokolovskiy, "Magnetocaloric effect in Ni-Mn-X (X = Ga, In, Sn, Sb) Heusler alloys," *The Physics of Metals and Metallography*, vol. 112, no. 7, pp. 633–665, dec 2011. [Online]. Available: http://link.springer.com/10.1134/S0031918X11070052

[6] J. Liu, T. Gottschall, K. P. Skokov, J. D. Moore, and O. Gutfleisch, "Giant magnetocaloric effect driven by structural transitions," *Nature Materials*, vol. 11, no. 7, pp. 620–626, jul 2012. [Online]. Available: http://www.nature.com/articles/nmat3334

[7] G. H. Yu, Y. L. Xu, Z. H. Liu, H.-M. Qiu, Z. Y. Zhu, X. P. Huang, and L. Q. Pan, "Recent progress in Heusler-type magnetic shape memory alloys," *Rare Metals*, vol. 34, no. 8, pp. 527–539, aug 2015. [Online]. Available: http://link.springer.com/10.1007/s12598-015-0534-1

[8] J. Romero Gómez, R. Ferreiro Garcia, A. De Miguel Catoira, and M. Romero Gómez, "Magnetocaloric effect: A review of the thermodynamic cycles in magnetic refrigeration," *Renewable and Sustainable Energy Reviews*, vol. 17, pp. 74–82, jan 2013. [Online]. Available: https://www.sciencedirect.com/science/article/pii/S136403211200528X

[9] J. Ortn and L. Delaey, "Hysteresis in shape-memory alloys," *International Journal of Non-Linear Mechanics*, vol. 37, no. 8, pp. 1275–1281, dec 2002. [Online]. Available: https://www.sciencedirect.com/science/article/pii/S0020746202000276

[10] V. Sokolovskiy, M. Zagrebin, V. Buchelnikov, and P. Entel, "Monte Carlo Simulations of Thermal Hysteresis in Ni-Mn-Based Heusler Alloys," *physica status solidi (b)*, vol. 255, no. 2, p. 1700265, feb 2018. [Online]. Available: http://doi.wiley.com/10.1002/pssb.201700265

[11] J. Mohd Jani, M. Leary, A. Subic, and M. A. Gibson, "A review of shape memory alloy research, applications and opportunities," *Materials & Design (1980-2015)*, vol. 56, pp. 1078–1113, apr 2014. [Online]. Available: https://www.sciencedirect.com/science/article/pii/S0261306913011345

[12] G. B. Kauffman and I. Mayo, "The Story of Nitinol: The Serendipitous Discovery of the Memory Metal and Its Applications," *The Chemical Educator*, vol. 2, no. 2, pp. 1–21, jun 1997. [Online]. Available: http://link.springer.com/10.1007/s00897970111a

[13] M. Blume, V. J. Emery, and R. B. Griffiths, "Ising Model for the λ Transition and Phase Separation in He 3 - He 4 Mixtures," *Physical Review A*, vol. 4, no. 3, pp. 1071–1077, sep 1971. [Online]. Available: https://link.aps.org/doi/10.1103/PhysRevA.4.1071

[14] T. W. Burkhardt, "Equivalence of the p-degenerate and ordinary Blume-Emery-Griffiths models," *Physical Review B*, vol. 60, no. 17, pp. 12 502–12 503, nov 1999. [Online]. Available: https://link.aps.org/doi/10.1103/PhysRevB.60.12502

[15] P. A. Lindgård, "Reply to Equivalence of the p-degenerate and ordinary Blume-Emery-Griffiths models," *Physical Review B*, vol. 60, no. 17, pp. 12 504–12 504, nov 1999. [Online]. Available: https://link.aps.org/doi/10.1103/PhysRevB.60.12504

[16] E. Vives, T. Castán, and P.-A. Lindgård, "Degenerate Blume-Emery-Griffiths model for the martensitic transformation," *Physical Review B*, vol. 53, no. 14, pp. 8915–8921, apr 1996. [Online]. Available: https://link.aps.org/doi/10.1103/PhysRevB.53.8915

[17] W. Ito, Y. Imano, R. Kainuma, Y. Sutou, K. Oikawa, and K. Ishida, "Martensitic and Magnetic Transformation Behaviors in Heusler-Type NiMnIn and NiCoMnIn Metamagnetic Shape Memory Alloys," *Metallurgical and Materials Transactions A*, vol. 38, no. 4, pp. 759–766, jun 2007. [Online]. Available: http://link.springer.com/10.1007/s11661-007-9094-9

[18] T. Castán, E. Vives, and P. A. Lindgård, "Modeling premartensitic effects in Ni 2 MnGa : A mean-field and Monte Carlo simulation study," *Physical Review B*, vol. 60, no. 10, pp. 7071–7084, sep 1999. [Online]. Available: https://link.aps.org/doi/10.1103/PhysRevB.60.7071

[19] V. D. Buchelnikov, V. V. Sokolovskiy, S. V. Taskaev, V. V. Khovaylo, A. A. Aliev, L. N. Khanov, A. B. Batdalov, P. Entel, H. Miki, and T. Takagi, "Monte Carlo simulations of the magnetocaloric effect in magnetic Ni-Mn-X (X = Ga, In) Heusler alloys," *Journal of Physics D: Applied Physics*, vol. 44, no. 6, p. 064012, feb 2011. [Online]. Available: http://stacks.iop.org/0022-3727/44/i=6/a=064012?key=crossref.40671d5350b66699f1de36427af2d5e0

[20] V. Sokolovskiy, V. Buchelnikov, K. Skokov, O. Gutfleisch, D. Karpenkov, Y. Koshkid'ko, H. Miki, I. Dubenko, N. Ali, S. Stadler, and V. Khovaylo, "Magnetocaloric and magnetic properties of Ni2Mn1-X CuXGa Heusler alloys: An insight from the direct measurements and ab initio and Monte Carlo calculations," *Journal of Applied Physics*, vol. 114, no. 18, p. 183913, nov 2013. [Online]. Available: http://aip.scitation.org/doi/10.1063/1.4826366

[21] V. Sokolovskiy, A. Grünebohm, V. Buchelnikov, and P. Entel, "Ab Initio and Monte Carlo Approaches For the Magnetocaloric Effect in Co- and In-Doped Ni-Mn-Ga Heusler Alloys," *Entropy*, vol. 16, no. 9, pp. 4992–5019, sep 2014. [Online]. Available: http://www.mdpi.com/1099-4300/16/9/4992

[22] V. V. Sokolovskiy, P. Entel, V. D. Buchelnikov, and M. E. Gruner, "Achieving large magnetocaloric effects in Co- and Cr-substituted Heusler alloys: Predictions from first-principles and Monte Carlo studies," *Physical Review B*, vol. 91, no. 22, p. 220409, jun 2015. [Online]. Available: https://link.aps.org/doi/10.1103/PhysRevB.91.220409

[23] Y. Sutou, Y. Imano, N. Koeda, T. Omori, R. Kainuma, K. Ishida, and K. Oikawa, "Magnetic and martensitic transformations of NiMnX(X=In,Sn,Sb) ferromagnetic shape memory alloys," *Applied Physics Letters*, vol. 85, no. 19, p. 4358, nov 2004. [Online]. Available: http://scitation.aip.org/content/aip/journal/apl/85/19/10.1063/1.1808879

[24] G. Kresse and J. Furthmüller, "Efficient iterative schemes for ab initio total-energy calculations using a plane-wave basis set," *Physical Review B*, vol. 54, no. 16, pp. 11 169–11 186, oct 1996. [Online]. Available: https://link.aps.org/doi/10.1103/PhysRevB.54.11169

[25] G. Kresse and J. Furthmüller, "Efficiency of ab-initio total energy calculations for metals and semiconductors using a plane-wave basis set," *Computational Materials Science*, vol. 6, no. 1, pp. 15–50, jul 1996. [Online]. Available: https://www.sciencedirect.com/science/article/pii/0927025696000080

[26] G. Kresse and J. Hafner, "Ab initio molecular dynamics for liquid metals," *Physical Review B*, vol. 47, no. 1, pp. 558–561, jan 1993. [Online]. Available: https://link.aps.org/doi/10.1103/PhysRevB.47.558

[27] G. Kresse and J. Hafner, "Ab initio molecular-dynamics simulation of the liquid-metalamorphous-semiconductor transition in germanium," *Physical Review B*, vol. 49, no. 20, pp. 14 251–14 269, may 1994. [Online]. Available: https://link.aps.org/doi/10.1103/PhysRevB.49.14251

[28] G. Kresse and D. Joubert, "From ultrasoft pseudopotentials to the projector augmented-wave method," *Physical Review B*, vol. 59, no. 3, pp. 1758–1775, jan 1999. [Online]. Available: https://link.aps.org/doi/10.1103/PhysRevB.59.1758

[29] P. E. Blöchl, "Projector augmented-wave method," *Physical Review B*, vol. 50, no. 24, pp. 17 953–17 979, dec 1994. [Online]. Available: https://link.aps.org/doi/10.1103/PhysRevB.50.17953

[30] M. B. Bouabci and C. E. I. Carneiro, "Eliminating metastability in first-order phase transitions," *Physical Review B*, vol. 54, no. 1, pp. 359–363, jul 1996. [Online]. Available: https://link.aps.org/doi/10.1103/PhysRevB.54.359

[31] A. Rachadi and A. Benyoussef, "Mixed cluster Monte Carlo algorithms for the Blume-Emery-Griffiths model," *Physical Review B*, vol. 68, no. 6, p. 064113, aug 2003. [Online]. Available: https://link.aps.org/doi/10.1103/PhysRevB.68.064113

[32] A. Ghosh and K. Mandal, "Effect of structural disorder on the magnetocaloric properties of Ni-Mn-Sn alloy," *Applied Physics Letters*, vol. 104, no. 3, p. 031905, jan 2014. [Online]. Available: http://aip.scitation.org/doi/10.1063/1.4862431